Research Square

Preprints are preliminary reports that have not undergone peer review.
They should not be considered conclusive, used to inform clinical practice,
or referenced by the media as validated information.

Junction-engineered halide perovskite neuronal arrays with on-chip physical time surfaces for spatiotemporal computing

Ho Won Jang

hwjang@snu.ac.kr

Seoul National University https://orcid.org/0000-0002-6952-7359

Youngmin Kim

Seoul National University

Hyeon Ji Lee

Seoul national university https://orcid.org/0009-0002-3299-4604

Kwan Woo Song

Seoul national university

Jinwoo Oh

Hongik University

Seung Ju Kim

USC https://orcid.org/0009-0000-0405-803X

Sung Woo Park

Seoul national university

Yuan Li

Huazhong University of Science and Technology https://orcid.org/0000-0001-7452-1149

Yongwoo Kwon

Hongik university

Article

Keywords:

Posted Date: November 18th, 2026

DOI: https://doi.org/10.21203/rs.3.rs-11442592/v1

License: This work is licensed under a Creative Commons Attribution 4.0 International License.
Read Full License

Additional Declarations: There is **NO** Competing Interest.

Article type: Research Article

Junction-engineered halide perovskite neuronal arrays with on-chip physical time surfaces for spatiotemporal computing

*Youngmin Kim[‡1], Hyeon Ji Lee[‡1], Kwan Woo Song[1], Jinwoo Oh[2], Seung Ju Kim[3], Sung Woo Park[1], Yuan Li[4], Yongwoo Kwon[*2], Ho Won Jang[*1,5]*

‡ These authors contributed equally to this work

[1]Department of Materials Science and Engineering, Research Institute of Advanced Materials, Seoul National University, Seoul 08826, Republic of Korea

[2]Department of Materials Science and Engineering, Hongik University, Seoul 04066, Republic of Korea

[3]Ming Hsieh Department of Electrical and Computer Engineering, University of Southern California, Los Angeles California 90089, United States

[4]State Key Laboratory of Material Processing and Die & Mould Technology, School of Materials Science and Engineering, Huazhong University of Science and Technology, Wuhan 430074, P. R. China

[5]Advanced Institute of Convergence Technology, Seoul National University, Suwon 16229, Republic of Korea

*Correspondence to: ykwon722@hongik.ac.kr, hwjang@snu.ac.kr

Abstract

Event-driven neuromorphic hardware requires reliable neuronal arrays that retain recent sensory history over a controlled temporal window. Here, we report on-chip physical time surfaces in two-dimensional Dion–Jacobson halide perovskite neuronal arrays. Nanoscale sidewall junctions confine ionic migration, enabling low-voltage volatile switching with reduced variability and no external current-compliance circuitry. Junction widths are scaled down to 5 nm, and processing below 100 °C enables fabrication on 4-inch wafers. The films retain crystallographic stability for more than two years. Residual ionic states support temporal integration and history-dependent firing. A 32 × 32 crossbar array represents changes in object position and apparent size through self-decaying conductance traces. Computational evaluation shows that controlled relaxation improves vehicle-motion prediction by preserving recent motion history and limiting interference from earlier activity. The results link nanoscale ionic confinement to reliable neuronal arrays and physical temporal processing for spatiotemporal computing.

Main

The growing demand for event-driven artificial intelligence (AI) is reshaping the requirements of computing hardware. [1-5] Emerging AI applications increasingly involve sparse and asynchronous signals in which information is encoded by the timing and correlation of events. [6-13] Efficient processing of such signals requires hardware elements that respond to individual events while retaining transient information about preceding activity. [14, 15] Artificial neurons based on volatile switching offer a compact means of processing temporal information through firing, relaxation and history-dependent excitability. [16-18] Extending such functionality to large, densely integrated arrays requires reproducible firing and recovery across devices, as compensating for temporal variability with dedicated circuitry at individual crosspoints would incur substantial area and interconnect overhead. [19, 20]

Threshold-switching (TS) devices provide a physical basis for neuronal activation and recovery through reversible transitions between high- and low-resistance states. [21-31] In diffusive memristors, metal-ion migration and spontaneous redistribution enable low-voltage volatile filamentary conduction, while residual ionic configurations retain stimulation history and influence subsequent switching. [30, 32-34] Such transient states support temporal integration and have been used to construct physical time surfaces for event-based processing. Reliable operation, however, depends on reproducible filament formation and dissolution. Spatial and electrical variations can drive uncontrolled ion redistribution, broaden threshold-voltage distributions and eventually degrade volatile switching. [35-37] External current compliance can suppress irreversible filament growth, but the required circuitry complicates dense crossbar-array (CBA) integration. Intrinsic regulation of filament evolution is therefore important for translating diffusive neuronal behaviour into reliable array operation.

Halide perovskites provide an ionic medium for diffusive neurons because their soft lattices support low-voltage metal-ion migration and reversible filamentary conduction. [38-42] Layered halide perovskites further allow ion transport to be regulated through alternating inorganic frameworks and organic spacer layers. [43, 44] Dion–Jacobson (DJ) perovskites are particularly attractive because diammonium spacers directly bridge adjacent inorganic layers, producing robust frameworks with anisotropic ion-transport environments. [45, 46] Crystallographic regulation alone, however, does not define the spatial extent of filament formation when the junction area greatly exceeds the filament dimensions. Sidewall-defined junctions provide complementary geometrical control by defining the switching dimension through the thickness of an ultrathin bottom electrode (BE), rather than the lateral electrode-overlap area. [47-49] Combining layered ionic media with sidewall junctions therefore offers a route to confining filament evolution while retaining compatibility with CBA integration.

Here, we present diffusive neuronal arrays based on two-dimensional (2D) DJ halide perovskites with nanoscale sidewall junctions. Preferentially oriented perovskite layers provide anisotropic ion-transport environments, while an ultrathin BE geometrically confines the active switching region. Combining crystallographic regulation with geometrical confinement enables low-voltage volatile switching with reduced variability and sustained operation without external current compliance. The sidewall architecture supports nanoscale junction scaling and fabrication on 4-inch wafers at temperatures no higher than 100 °C. We demonstrate operation in crossbar arrays comprising up to 32 × 32 devices, where transient ionic states encode recent spatial input history as physical time surfaces. Numerical motion analysis further illustrates how temporal persistence influences motion inference, linking reliable diffusive neuronal arrays to spatiotemporal computing.

Three-dimensional junction engineering for reliable diffusive neurons

Artificial neurons for event-driven neuromorphic hardware require input accumulation, threshold firing and post-fire recovery to process temporally structured signals. [50] Diffusive memristors natively implement such functions through the coupled drift and diffusion of metal ions (**Fig. 1a**). Electrical excitation drives Ag migration to form transient conductive filaments, whereas spontaneous ion diffusion after stimulus removal restores the high-resistance state. Incomplete relaxation leaves residual conductive nuclei that facilitate subsequent filament formation, thereby enabling temporal accumulation (**Fig. 1b**). Reliable operation in dense diffusive neuronal arrays therefore requires reproducible formation and dissolution of volatile filaments within a confined switching volume. Conventional CBAs employ overlap junctions with large active areas, allowing stochastic filament nucleation over broad junction volumes (**Fig. 1c**). Such spatial freedom amplifies the influence of local ionic disorder and electric-field inhomogeneity, resulting in large switching variations. To address this limitation, we employ three-dimensional junction engineering (**Fig. 1d**). Preferentially oriented DJ perovskites provide anisotropic ion-transport pathways, while a sidewall-defined junction formed by an ultrathin bottom electrode confines filament evolution to a nanoscale switching volume. Within the 2D DJ framework, alternating inorganic halide layers and diammonium spacer molecules guide Ag-ion migration along crystallographically preferred pathways (**Fig. 1e**). At the same time, the switching dimension is defined by the thickness of the bottom electrode rather than by the lateral junction area. In contrast to conventional crosspoint junctions, which permit multidirectional filament growth over large active regions (**Fig. 1f**), the three-dimensional sidewall architecture confines volatile filament formation to a well-defined nanoscale volume. Such confinement suppresses irreversible filament overgrowth and promotes reproducible filament formation and spontaneous dissolution (**Fig. 1g**), enabling stable volatile switching and autonomous post-fire recovery.

Device architecture for reliable volatile switching

We implemented this junction engineering strategy by fabricating and structurally evaluating a sidewall-confined 2D DJ halide perovskite neuron. The active layer consists of butane-1,4-diammonium lead iodide (BDA-PbI_4), in which the layered PbI_6 octahedral framework provides anisotropic ion-transport environments (**Fig. 2a**). Specifically, BDA-PbI_4 was spin-coated on a SiO_2/Pt/SiO_2 BE stack and contacted by cross-line Ag/Au top electrodes (**Fig. 2b**). Here, the Ag layer supplies the mobile ions for diffusive switching, whereas the Au overlayer limits direct Ag exposure to ambient conditions. The exposed Pt sidewall precisely defines the metal/perovskite junction, thereby confining the active switching region near the ultrathin BE edge. Cross-sectional energy-dispersive X-ray spectroscopy (EDS) verified that Au, Ag, I, Pt, Si and O were spatially distributed according to the designed sidewall structure (**Fig. 2c**). High-resolution transmission electron microscopy (HRTEM) and fast Fourier transform (FFT) analysis confirmed that crystalline BDA-PbI_4 was preserved near the junction, with a lattice spacing of 0.63 nm assigned to the (10-1) plane (**Fig. 2d**). Photoluminescence (PL), ultraviolet–visible (UV–Vis) absorption and scanning electron microscopy (SEM) measurements further verified the characteristic optical response and continuous film morphology of BDA-PbI_4 (**Supplementary Figs. 1** and **2**). X-ray diffraction (XRD) measurements showed that the characteristic layered orientation of BDA-PbI_4 was retained after more than two year of storage (**Fig. 2e**). Grazing-incidence wide-angle X-ray scattering (GIWAXS) further confirmed the persistence of preferential crystallographic orientation in the BDA-PbI_4 film after more than 1.5 years of storage (**Supplementary Fig. 3**). The sidewall architecture was fabricated using processes below 100 °C and is compatible with wafer-scale integration. Electrical characterization of 16 spatially distributed regions across a 4-inch wafer demonstrated uniform operating characteristics (**Supplementary Fig. 4**).

The devices exhibited asymmetric volatile TS without external current compliance (**Fig. 2f**), consistent with self-limited conductive-path formation within the sidewall junction. Volatile operation was preserved after more than one year of ambient storage (**Supplementary Fig. 5**). Reducing the sidewall width from 100 to 25 and 10 nm lowered the mean threshold voltage from 204 to 148.5 and 81.9 mV, respectively, while reducing the corresponding standard deviation (SD) from 54.3 to 15.49 and 4.7 mV (**Fig. 2g–i**). Junction scaling therefore enabled sub-100-mV switching with reduced threshold-voltage variability. Devices with a reversed electrode configuration exhibited opposite switching polarity and a higher threshold voltage, suggesting that electrode geometry affects Ag-ion supply and filament nucleation at the sidewall junction (**Supplementary Fig. 6**). Reference structures without sidewall confinement exhibited stochastic and non-volatile switching, supporting the role of the sidewall junction in achieving reproducible volatile operation (**Supplementary Fig. 7**).

Migration energetics and junction geometry for reliable volatile switching

We performed density functional theory (DFT) calculations and nudged elastic band (NEB) analysis to examine Ag migration in layered BDA-PbI_4. Migration between neighbouring framework-associated apical iodide pockets, AP1 and AP2, exhibited an activation barrier of 0.646 eV, comparable to previously reported values for Ag migration in halide perovskites (**Fig. 3a**). [43, 51-53] AP2 was 0.022 eV lower in energy than AP1, indicating comparable energetic stability of the neighbouring apical-pocket configurations. By contrast, the spacer-side configuration, SV, was 0.247 eV higher in energy than AP1, indicating less favourable Ag occupation near the organic spacer. The relative configuration energies and transition-state energies of the separately calculated AP2–AP1, AP1–SV and SV–SV2 pathways are summarized in **Supplementary Fig. 8**.

Although the AP1-to-SV pathway exhibited a lower forward barrier of 0.313 eV, the reverse barrier derived from the same NEB pathway was only 0.065 eV. The higher energy of SV and the low reverse barrier favour return to AP1 over persistent occupation of SV under the calculated zero-field conditions (**Fig. 3b**). Ag can therefore access the spacer-side site without being energetically favoured to remain there. The AP1-to-SV pathway represents a local excursion towards the organic spacer rather than a complete migration pathway across the organic layer. Consequently, the low forward barrier alone does not establish facile interlayer transport, which also depends on subsequent migration steps. The calculated energy landscape supports preferential Ag occupation in framework-associated iodide pockets and facile return from SV, providing an energetic basis for interpreting the experimentally observed confinement of filament switching. Detailed site configurations and migration pathways are provided in **Supplementary Figs. 9** and **10**.

We then used 3D phase-field simulations based on the proposed device structures to examine how sidewall geometry affects Ag-filament evolution during the set process. In the simulations, the normalized phase-field order parameter represented the degree of Ag-rich conductive filament formation and was coupled with electrostatic potential calculations. The simulated wide-junction geometry represented a conventional device with L/d = 1/4, whereas the sidewall-defined geometry represented the proposed confined device with L/d = 2. The Ag-species distributions showed that the wide-junction geometry promoted laterally dispersed Ag redistribution across the active layer, whereas the sidewall-defined geometry localized Ag accumulation near the nanoscale BE region (**Fig. 3c**). The corresponding phase-field and temperature maps further revealed extensive Ag-rich conductive-path formation and a pronounced thermal hotspot in the wide-junction geometry, while both filament evolution and heat generation remained spatially confined in the sidewall-defined geometry (**Fig. 3d**). The

reduced switching-voltage variability in the sidewall-defined geometry further supports the role of geometrical confinement in stabilizing volatile switching (**Supplementary Fig. 11**). These results indicate that geometrical confinement confines Ag-filament evolution and suppresses excessive conductive-path formation, thereby supporting reproducible volatile switching.

The effect of junction geometry was experimentally evaluated by varying the BE width, which defines the effective switching dimension. Devices with nanoscale BE widths showed markedly reduced subthreshold current and low threshold voltage, indicating suppression of parasitic conductive pathways while maintaining low-voltage switching (**Fig. 3e**). Repeated pulse measurements demonstrated stable volatile switching over more than 10^6 cycles, indicating that the sidewall-confined switching pathway remains recoverable during long-term operation (**Fig. 3f**). We compared switching endurance across device geometries to connect confinement with repeated volatile operation (**Fig. 3g**). Dot-type and conventional crosspoint devices showed faster degradation as the effective switching area increased, whereas the sidewall-confined stacked device preserved volatile switching under repeated cycling. Benchmarking against reported volatile TS devices is summarized in **Fig. 3h**. The detailed comparison in **Supplementary Table 1** shows that the stacked 2D halide perovskite neuron combines low operating field, compliance-free switching, high endurance and CBA compatibility. These comparisons support the role of three-dimensional junction engineering in achieving reliable volatile switching for diffusive neuronal operation.

Self-decaying ionic states encode recent firing history

We examined how sidewall-confined volatile switching retains recent stimulation through transient ionic states. Electrical excitation redistributes Ag species towards a conductive pathway, whereas spontaneous relaxation after stimulus removal restores the high-resistance

state (**Fig. 4a**). Incomplete relaxation can leave residual Ag-rich configurations near the sidewall junction, reducing the excitation required for subsequent firing before full recovery. Under a constant bias of 0.6 V with a 10 MΩ series resistor, the output current increased abruptly after a millisecond-scale delay (**Fig. 4b**), consistent with gradual ionic redistribution preceding conductive-path formation. Additional measurements resolved delayed firing, intermittent firing near the firing boundary and increasing output current under continued stimulation (**Supplementary Fig. 12a-c**). Time-of-flight secondary-ion mass spectrometry (TOF-SIMS) revealed pulse-count-dependent Ag enrichment in the halide perovskite switching layer, supporting cumulative Ag redistribution during repeated stimulation (**Supplementary Fig. 13**). [30] Repeated voltage pulses of identical amplitude produced an accumulation-to-firing transition, reproducing leaky integrate-and-fire behaviour (**Fig. 4c**). Repeated pulse-train measurements confirmed the reproducibility of the transition (**Supplementary Fig. 14**). Firing statistics were evaluated using trains of 2,500 pulses, including measurements with a pulse duration of 1 ms. Varying the pulse voltage and duration revealed a systematic voltage–time dependence of firing probability (**Fig. 4d**). Shorter pulses required higher voltages to achieve the same firing probability, consistent with time-dependent ionic redistribution under electrical stimulation.

To assess sustained temporal processing, we performed a device-aware spoken-digit classification benchmark using the Spiking Heidelberg Digits (SHD) dataset (**Fig. 4e**). [54, 55] [56, 57] Auditory events were converted into 100 × 160 binary spike tensors (**Supplementary Fig. 15**), and device degradation was introduced only during inference to isolate the effect of cumulative neuronal firing after readout training. Classification accuracy progressively decreased under the unconfined switching condition, whereas the confined condition maintained high accuracy over repeated firing (**Fig. 4f**). The corresponding confusion matrices

showed greater classification errors under the unconfined condition (**Fig. 4g,h**), supporting the importance of switching reliability for sustained temporal processing. In addition, the same DJ halide perovskite platform also supports analogue synaptic switching through electrode reconfiguration, indicating material compatibility for integrated synaptic and neuronal functions (**Supplementary Fig. 16**). [14] This material-level versatility provides a common platform for both analogue synaptic weight modulation and transient neuronal processing. In the neuronal mode, volatile relaxation creates self-decaying states that retain recent stimulation while autonomously erasing older information, providing the physical basis for the time surfaces used in temporal-attention computing.

Physical time surfaces for spatiotemporal processing

We next examined history-dependent firing in a 7 × 7 CBA, where transient ionic states provide local temporal context for subsequent inputs. In event-driven neuromorphic systems, recent activity within a local receptive field helps interpret subsequent events. [58, 59] Volatile ionic relaxation provides a physical mechanism for retaining preceding activity and temporarily modulating neuronal excitability. A photograph and an enlarged optical micrograph show the fabricated array (**Fig. 4i**). Narrow device-to-device threshold-voltage distributions supported collective array operation (**Supplementary Figs. 17** and **18**), while additional measurements indicated limited parasitic-current contributions from neighbouring cells (**Supplementary Fig. 19**). Sequential X- and Y-shaped voltage patterns were applied to the array (**Fig. 4j**), and the corresponding output-current maps resolved history-dependent responses (**Fig. 4k**). Subthreshold stimulation of the pristine array produced no detectable firing. Following suprathreshold activation of an X-shaped pattern, a subthreshold Y-shaped input elicited firing only at cells overlapping with the preceding activation. Suprathreshold Y-shaped stimulation subsequently activated the entire pattern, with enhanced responses at previously activated cells.

After 50 ms of relaxation, subthreshold stimulation again produced no detectable firing. Selective sensitization, response amplification and recovery demonstrate that preceding activity can modulate spatially distributed neuronal responses within a transient temporal window.

On-chip physical time surfaces for motion encoding and prediction

Interpreting a changing visual scene requires temporal context to resolve object motion and anticipate subsequent changes. Recent observations must remain accessible long enough to distinguish changes, while older activity must decay to avoid obscuring the current trajectory. [60-62] We implemented physical time surfaces in a 32 × 32 neuronal CBA using spatially distributed volatile device states to represent recent input history (Supplementary Fig. 20a–c). Neuronal relaxation defines the temporal window over which preceding stimulation influences subsequent responses (**Fig. 5a**). For sequential spatial inputs, transient traces retain preceding object positions, whereas prolonged persistence can superimpose activity from earlier positions (**Fig. 5b**). We examined the encoding principle in the fabricated array (**Fig. 5c**) by applying sequential spatial inputs and measuring the resulting conductance maps (**Fig. 5d**). Each event was applied using a 1 V, 10 ms pulse, followed immediately by a 0.25 V, 10 ms trace-readout pulse. The readout voltage was below the firing threshold of fully relaxed devices but could elicit firing when sufficient residual activity remained. Weaker residual states produced conductance responses without firing, whereas devices without preceding events showed no event-induced enhancement. The measured maps therefore captured the spatial distribution of history-dependent conductance responses. For static, rightward-moving and receding-object patterns, the conductance profiles retained information about both the current input and preceding activation (**Fig. 5e**). Comparing successive profiles resolved lateral displacement and changes in spatial extent, demonstrating array-level encoding of recent spatial input history.

To examine how temporal persistence influences motion inference, we performed a proof-of-concept simulation using a vehicle sequence from the GOT-10k dataset. [63] Frame-wise vehicle positions and apparent sizes were encoded into exponentially relaxing temporal states, allowing recent motion information to be retained over different temporal windows. Shorter persistence emphasized recent vehicle positions, whereas prolonged persistence retained extended traces along preceding trajectories (**Fig. 5f**). Temporal feature states were used to forecast subsequent changes in horizontal position and apparent area, illustrating how recent motion history can support prediction of displacement and size change (**Fig. 5g**). Motion-classification accuracy depended on the relaxation time constant, reflecting a balance between retention of recent activity and interference from older traces (**Fig. 5h**). Features extracted from the relaxing temporal states were processed using a multilayer perceptron (MLP) to distinguish left, right, toward and away motion (**Fig. 5i**). Under the shorter-persistence condition, class recalls reached 92.3% and 85.1% for leftward and rightward motion, respectively, compared with 69.2% and 62.2% under the longer-persistence condition (**Fig. 5j**). For apparent away and toward motion, the corresponding recalls were 81.9% and 78.3%, compared with 62.1% and 68.5%, respectively (**Fig. 5k**). The results show that temporal persistence shapes motion-feature discriminability by balancing recent-history retention against interference from preceding activity. Together, the array measurements and computational evaluations highlight the role of transient states in spatial history encoding and the importance of matching temporal persistence to the input dynamics.

Discussion

The central contribution of the platform is the combination of crystallographic ion-transport regulation and nanoscale junction confinement for reliable diffusive neuronal arrays. Sidewall-defined switching regions reduce threshold-voltage variability and support repeated volatile

operation without external current compliance, while low-temperature processing enables fabrication on 4-inch wafers. Beyond individual-device switching, the 7 × 7 and 32 × 32 CBAs demonstrate history-dependent activation and physical encoding of recent spatial inputs through transient ionic states. Computational evaluations further illustrate how switching endurance and temporal persistence influence sustained classification and motion inference. Linking junction design, switching reliability and array-level temporal encoding provides a device-engineering basis for spatiotemporal computing. Further control of relaxation dynamics could extend the platform to a broader range of input timescales and hierarchical temporal processing.

Method

Materials preparation

Butane-1,4-diammonium iodide ($BDAI_2$, 99%) was purchased from Sigma-Aldrich. NH_4Cl (99%), *N*,*N*-dimethylformamide (DMF, 99.8%, anhydrous), and PMMA (acrylic) and chlorobenzene (99.8%, anhydrous) were prepared from Sigma-Aldrich. Lead(II) iodide (PbI_2, 99.9985%) was obtained from Alfa Aesar.

2D DJ Halide perovskite solution preparation

The 2D DJ-phase perovskite precursor solution ($BDAPbI_4$) was prepared by dissolving $BDAI_2$, PbI_2, and NH_4Cl powders in a 1:1:0.1 molar ratio in 1 ml anhydrous DMF, followed by stirring at 80 °C for 24 h.

Device fabrication

Si substrates with 300 nm SiO_2 were sequentially cleaned with acetone, isopropanol, and deionized water under ultrasonication. Patterned BE substrates were fabricated by sequential electron beam evaporation of 25 nm SiO_2, 2 nm Ti, Pt, 2 nm Ti, and 25 nm SiO_2 at room temperature under 1×10^{-6} Torr, where Ti served as an adhesion layer. After UV ozone treatment for 30 min, the 2D precursor solution was spin coated onto the patterned substrates at 5000 rpm for 45 s. Chlorobenzene antisolvent (130 μL) was dropped 10 s after spin coating began, followed by annealing at 100 °C for 15 min. After cooling to room temperature, PMMA in chlorobenzene (5 mg mL^{-1}) was spin coated onto the 2D film at 5000 rpm for 45 s. Finally, 25 nm Ag top electrodes and a 10 nm Au passivation layer were sequentially deposited by electron beam evaporation through a shadow mask.

Materials characterization

XRD patterns were collected at room temperature using an X-ray diffractometer (D8 Advance, Bruker) with Cu Kα radiation (λ = 1.54056 Å). The measurements were performed over a 2θ range of 3–50° with a scan speed of 5° min−1 and a step size of 0.02°. GIWAXS measurements were conducted using a Xeuss 2.0 system (Xenocs) equipped with a PILATUS 300K detector (Dectris), with Cu Kα radiation (λ = 1.54189 Å) at an incidence angle of 0.5°. PL spectra were acquired at room temperature using a fluorescence spectrophotometer (FluoTime 300, PicoQuant) with excitation at 520 nm and collected over a wavelength range of 600–850 nm. Surface and cross-sectional film morphologies were examined using a field-emission SEM (MERLIN Compact, ZEISS). Images were acquired with an in-lens secondary electron detector at an accelerating voltage of 5 kV. Atomic-scale nanostructures were further analysed using a high-resolution TEM (JEM-2100F, JEOL) operated at 200 kV.

Electrical characterization

The electrical properties were measured with Agilent 4156c and Keithley 4200A semiconductor analysers in the direct current voltage-sweeping mode. The Keithly 4200A has a high-resolution pre-amplifier with source measure unit, 4225-pulse measure unit (PMU) and 4225-remote preamplifier/switch module (RPM) remote amplifier. Keithley 4200A-SCS, Keithley 2636A, Keithley 4225-PMU pulse generator and 4225-RPM amplifier were used to measure synaptic plasticity on the basis of the alternate current pulse mode. All electrical characterizations were performed with the BE grounded. All electrical measurements were performed under dark conditions.

Computational details

DFT calculations were performed using the Vienna Ab initio Simulation Package (VASP) with the projector augmented-wave (PAW) method. Non-spin-polarized calculations were performed using the generalized gradient approximation (GGA) with the Perdew–Burke–

Ernzerhof (PBE) exchange–correlation functional. Dispersion interactions were included using DFT-D3 with Becke–Johnson damping. A plane-wave cutoff energy of 520 eV, a 2 × 2 × 1 supercell and a Γ-centred 2 × 2 × 1 k-point mesh were used. The pristine host was fully relaxed by optimizing the lattice parameters and atomic positions. Ag-containing structures were constructed by introducing one Ag atom into the optimized supercell and modelling Ag^+ by removing one electron. The lattice parameters were fixed to those of the optimized host, and all atomic positions were relaxed until the residual forces were below 0.02 eV $Å^{-1}$. Migration barriers between representative AP and spacer-associated Ag sites were calculated using the climbing-image nudged elastic band (CI-NEB) method with five intermediate images generated by image-dependent pair potential (IDPP) interpolation.

Multiphysics simulation.

Three-dimensional device simulations were conducted in COMSOL Multiphysics using a phase-field model coupled with electrostatic potential calculations. The normalized phase-field order parameter, φ, represented the degree of Ag-rich conductive filament formation. Ag-filament evolution was simulated in planar and geometrically confined memristor geometries using scaled dimensions that preserved the relative device architecture, with the confined model incorporating a restricted BE region.

Auditory classification benchmark

Device-aware auditory classification was evaluated using the SHD dataset. Raw auditory spike events were normalized in time, discretized into 100 temporal bins, and compressed from 700 cochlear channels to 160 auditory channels to generate binary spike tensors of size 100 × 160. The processed spike tensors were used to train a temporal neural readout for spoken-digit classification (digits 0–9). After training, all network parameters were fixed, and device degradation was introduced only during inference according to the experimentally measured

endurance characteristics of each neuron architecture. Classification accuracy and confusion matrices were subsequently evaluated as a function of cumulative firing events.

Device-informed simulation of a one-neuron–one-synapse spiking neural network

Firing-rate-coded SNN simulations were performed using a time-stepped multilayer perceptron composed of leaky integrate-and-fire neurons. Experimentally measured neuron and synapse characteristics were incorporated to construct a 1N–1S unit comprising a neuron device and a synaptic device. The network consisted of an input layer, a single hidden layer and a ten-neuron output layer for MNIST classification. Input images were encoded as Bernoulli spike trains, and the synaptic weights were trained using surrogate-gradient backpropagation. Device non-idealities were incorporated by limiting the available spike budget according to the experimentally measured endurance of each neuron-device architecture. Classification accuracy was evaluated as a function of training epoch and compared with that of an ideal numerical model without endurance constraints.

Motion forecasting and classification using physical time surfaces

A proof-of-concept motion-analysis simulation was performed using the 421-frame GOT-10k_Val_000179 vehicle sequence with an assigned frame interval of 0.1 s. Frame-wise reference bounding boxes provided the vehicle centre coordinates (x_t, y_t) and apparent area A_t, from which the feature vector was defined as $\boldsymbol{f}_t = (x_t, y_t, \ln\sqrt{A_t})$. Frame-to-frame changes were integrated into exponentially relaxing temporal states according to $\boldsymbol{s}_t = \alpha\boldsymbol{s}_{t-1} + (1 - \alpha)(\boldsymbol{f}_t - \boldsymbol{f}_{t-1})$, where $\alpha = \exp(-\Delta t/\tau)$. Subsequent features were forecast as $\hat{\boldsymbol{f}}_{t+h} = \boldsymbol{f}_t + h\boldsymbol{s}_t$, with h denoting the forecast horizon. Relaxation time constants of 0.1 and 1 s were used to represent different trace-persistence conditions, with an additional sweep from 0.025 to 10 s. For motion classification, the relaxing temporal states were supplied to a MLP with fully connected hidden layers and nonlinear activation. Horizontal and depth-related motion were evaluated independently as

left–right and apparent toward–away tasks. Classification performance was quantified using accuracy, class-specific recall and row-normalized confusion matrices.

References

1. Lanza, M., et al., *The growing memristor industry.* Nature, 2025. **640**(8059): p. 613-622.
2. Song, W., et al., *Programming memristor arrays with arbitrarily high precision for analog computing.* Science, 2024. **383**(6685): p. 903-910.
3. Aguirre, F., et al., *Hardware implementation of memristor-based artificial neural networks.* Nature communications, 2024. **15**(1): p. 1974.
4. Huang, Y., et al., *Memristor-based hardware accelerators for artificial intelligence.* Nature Reviews Electrical Engineering, 2024. **1**(5): p. 286-299.
5. Song, M.-K., et al., *Recent advances and future prospects for memristive materials, devices, and systems.* ACS nano, 2023. **17**(13): p. 11994-12039.
6. Kim, S.J., et al., *Self-powered analogue neuromorphic system for multimodal sensing, encoding and learning with diffusive and drift memristors.* Nature Sensors, 2026: p. 1-10.
7. Zhao, R., et al., *Memristive ion dynamics to enable biorealistic computing.* Chemical Reviews, 2024. **125**(2): p. 745-785.
8. Kim, Y., C.W. Lee, and H.W. Jang, *Neuromorphic hardware for artificial sensory systems: a review.* Journal of Electronic Materials, 2025. **54**(5): p. 3609-3650.
9. Yang, K., et al., *Nonlinearity in memristors for neuromorphic dynamic systems.* Small Science, 2022. **2**(1): p. 2100049.
10. Kumar, S., et al., *Dynamical memristors for higher-complexity neuromorphic computing.* Nature Reviews Materials, 2022. **7**(7): p. 575-591.
11. Zhong, B., et al., *Monolithic cell-on-memristor architecture enables wafer-scale integration of oscillatory chemoreceptors for bio-realistic gustatory chips.* Nature Materials, 2026: p. 1-10.
12. Han, J.K., et al., *Artificial olfactory neuron for an in-sensor neuromorphic nose.* Advanced Science, 2022. **9**(18): p. 2106017.
13. Kang, M., et al., *Neuromorphic olfaction with ultralow-power gas sensors and ovonic threshold switch.* Science Advances, 2025. **11**(39): p. eadv9222.
14. Eshraghian, J.K., et al., *Training spiking neural networks using lessons from deep learning.* Proceedings of the IEEE, 2023. **111**(9): p. 1016-1054.
15. Kim, Y., et al., *Programmable ferroelectric rectifier for reliable and efficient neuromorphic crossbar array.* Nature Communications, 2026.
16. Kim, Y. and H.W. Jang, *Designing memristive materials for artificial dynamic intelligence.* Advanced Intelligent Discovery, 2026. **2**(1): p. e202500020.
17. Kim, Y., et al., *Two-terminal neuromorphic devices for spiking neural networks: neurons, synapses, and array integration.* ACS nano, 2024. **18**(51): p. 34531-34571.
18. Lee, Y.J., et al., *Nanoelectronics using metal–insulator transition.* Advanced Materials, 2024. **36**(5): p. 2305353.
19. Yi, S.-i., et al., *Activity-difference training of deep neural networks using memristor crossbars.* Nature Electronics, 2023. **6**(1): p. 45-51.
20. Zhao, R., et al., *A spiking artificial neuron based on one diffusive memristor, one transistor and one resistor.* Nature Electronics, 2025: p. 1-11.
21. Ju, D. and S. Kim, *Versatile NbO_x-based volatile memristor for artificial intelligent applications.* Advanced Functional Materials, 2024. **34**(49): p. 2409436.
22. Milozzi, A., S. Ricci, and D. Ielmini, *Memristive tonotopic mapping with volatile resistive switching memory devices.* Nature Communications, 2024. **15**(1): p. 2812.

23. Wang, R., et al., *Recent advances of volatile memristors: Devices, mechanisms, and applications.* Advanced Intelligent Systems, 2020. **2**(9): p. 2000055.
24. John, R.A., et al., *Reconfigurable halide perovskite nanocrystal memristors for neuromorphic computing.* Nature communications, 2022. **13**(1): p. 2074.
25. Islam, M., et al., *An electro-optical Mott neuron based on niobium dioxide.* Nature Electronics, 2025. **8**(8): p. 672-679.
26. Kim, G., et al., *Mott neurons with dual thermal dynamics for spatiotemporal computing.* Nature materials, 2024. **23**(9): p. 1237-1244.
27. Kumar, S., J.P. Strachan, and R.S. Williams, *Chaotic dynamics in nanoscale NbO_2 Mott memristors for analogue computing.* Nature, 2017. **548**(7667): p. 318-321.
28. Kumar, S., R.S. Williams, and Z. Wang, *Third-order nanocircuit elements for neuromorphic engineering.* Nature, 2020. **585**(7826): p. 518-523.
29. Jeon, J.W., et al., *Vertically stackable ovonic threshold switch oscillator using atomic layer deposited $Ge_{0.6}Se_{0.4}$ film for high-density artificial neural networks.* ACS Applied Materials & Interfaces, 2024. **16**(12): p. 15032-15042.
30. Im, I.H., et al., *Halide perovskites-based diffusive memristors for artificial mechano-nociceptive system.* Advanced Materials, 2024. **36**(1): p. 2307334.
31. Yuan, R., et al., *A neuromorphic physiological signal processing system based on VO_2 memristor for next-generation human-machine interface.* Nature Communications, 2023. **14**(1): p. 3695.
32. Fu, T., et al., *Bioinspired bio-voltage memristors.* Nature communications, 2020. **11**(1): p. 1861.
33. Yoon, J.H., et al., *An artificial nociceptor based on a diffusive memristor.* Nature communications, 2018. **9**(1): p. 417.
34. Wang, Z., et al., *Memristors with diffusive dynamics as synaptic emulators for neuromorphic computing.* Nature materials, 2017. **16**(1): p. 101-108.
35. Im, I.H., et al., *Controlling threshold and resistive switch functionalities in Ag-incorporated organometallic halide perovskites for memristive crossbar array.* Advanced Functional Materials, 2023. **33**(8): p. 2211358.
36. Chekol, S.A., et al., *Effect of the threshold kinetics on the filament relaxation behavior of Ag-based diffusive memristors.* Advanced functional materials, 2022. **32**(15): p. 2111242.
37. Chekol, S.A., et al., *Strategies to control the relaxation kinetics of Ag-based diffusive memristors and implications for device operation.* Advanced Electronic Materials, 2022. **8**(11): p. 2200549.
38. Kim, H., et al., *Halide perovskites for applications beyond photovoltaics.* Small Methods, 2018. **2**(3): p. 1700310.
39. Kim, S.J., et al., *Halide Perovskites for Neuromorphic Sensing and Computing.* ACS Applied Materials & Interfaces, 2025. **17**(44): p. 59951-59978.
40. Kim, H., et al., *Halide perovskites for resistive random-access memories.* Journal of Materials Chemistry C, 2019. **7**(18): p. 5226-5234.
41. Choi, J., et al., *Organic–inorganic hybrid halide perovskites for memories, transistors, and artificial synapses.* Advanced materials, 2018. **30**(42): p. 1704002.
42. Im, I.H., et al., *A low-power filamentary memristor crossbar array enabled via cubic α-phase stabilized mixed-cation lead halide perovskites.* Journal of Materials Chemistry C, 2025. **13**(20): p. 10310-10320.
43. Kim, S.J., et al., *Linearly programmable two-dimensional halide perovskite memristor arrays for neuromorphic computing.* Nature Nanotechnology, 2025. **20**(1): p. 83-92.

44. Hong, K., et al., *Low-dimensional halide perovskites: review and issues.* Journal of Materials Chemistry C, 2018. **6**(9): p. 2189-2209.
45. He, D., et al., *Homogeneous 2D/3D heterostructured tin halide perovskite photovoltaics.* Nature Nanotechnology, 2025. **20**(6): p. 779-786.
46. Blancon, J.-C., et al., *Semiconductor physics of organic–inorganic 2D halide perovskites.* Nature nanotechnology, 2020. **15**(12): p. 969-985.
47. Son, K., et al., *Vertical Self-Rectifying Memristive Arrays for Page-Wise Parallel Logic and Arithmetic Processing.* Advanced Materials, 2026. **38**(8): p. e14099.
48. Han, J., et al., *Vertical Memristive Crossbar Array for Multilayer Graph Embedding and Analysis.* Advanced Materials, 2025. **37**(10): p. 2416988.
49. Lee, S.H., et al., *In-Materia Annealing and Combinatorial Optimization Based on Vertical Memristive Array.* Advanced Materials, 2024. **36**(40): p. 2410191.
50. Kandel, E.R., et al., *Principles of neural science*. Vol. 4. 2000: McGraw-hill New York.
51. Ji, Y., et al., *Ultralow energy adaptive neuromorphic computing using reconfigurable zinc phosphorus trisulfide memristors.* Nature Communications, 2025. **16**(1): p. 6899.
52. Li, Y., et al., *Memristors with analogue switching and high on/off ratios using a van der Waals metallic cathode.* Nature Electronics, 2025. **8**(1): p. 36-45.
53. Eames, C., et al., *Ionic transport in hybrid lead iodide perovskite solar cells.* Nature communications, 2015. **6**(1): p. 7497.
54. Theunissen, F.E. and J.E. Elie, *Neural processing of natural sounds.* Nature Reviews Neuroscience, 2014. **15**(6): p. 355-366.
55. Rieke, F., et al., *Spikes: exploring the neural code*. 1999: MIT press.
56. Cramer, B., et al., *The heidelberg spiking data sets for the systematic evaluation of spiking neural networks.* IEEE Transactions on Neural Networks and Learning Systems, 2020. **33**(7): p. 2744-2757.
57. Grüning, A. and S.M. Bohte. *Spiking neural networks: Principles and challenges*. in *ESANN*. 2014. Bruges.
58. Lagorce, X., et al., *Hots: a hierarchy of event-based time-surfaces for pattern recognition.* IEEE transactions on pattern analysis and machine intelligence, 2016. **39**(7): p. 1346-1359.
59. Ye, F., et al., *Diffusive memristors with uniform and tunable relaxation time for spike generation in event-based pattern recognition.* Advanced Materials, 2023. **35**(37): p. 2204778.
60. Ge, X., et al., *Retinal waves prime visual motion detection by simulating future optic flow.* Science, 2021. **373**(6553): p. eabd0830.
61. Benigno, G.B., et al., *Waves traveling over a map of visual space can ignite short-term predictions of sensory input.* Nature Communications, 2023. **14**(1): p. 3409.
62. Liu, B., et al., *Predictive encoding of motion begins in the primate retina.* Nature neuroscience, 2021. **24**(9): p. 1280-1291.
63. Huang, L., X. Zhao, and K. Huang, *Got-10k: A large high-diversity benchmark for generic object tracking in the wild.* IEEE transactions on pattern analysis and machine intelligence, 2019. **43**(5): p. 1562-1577.

Ethics declarations - Competing interests

The authors declare no competing interests.

Data availability

The data that support the conclusions of this study are available from the corresponding authors upon request.

Code availability

The code that used for the software simulation for this study is available from the corresponding authors upon request.

Acknowledgements

We thank Professor Qiangfei Xia for his helpful comments and valuable suggestions for improving the clarity of the manuscript. This research was supported by the Nano & Material Technology Development Program through the National Research Foundation of Korea (NRF) funded by Ministry of Science and ICT(RS-2024-00405016). This research was supported by the National Research Council of Science & Technology (NST) grant by the Korea government (MSIT) (No. GTL25021-000). This work was supported by the InnoCORE program of the Ministry of Science and ICT (1.250021.01). This work was supported by the National Research Foundation of Korea (NRF) funded by the Ministry of Science and ICT (MSIT), South Korea (RS-2024-00421181). The Inter-University Semiconductor Research Center and Institute of Engineering Research at Seoul National University provided research facilities for this work.

Figures and Captions

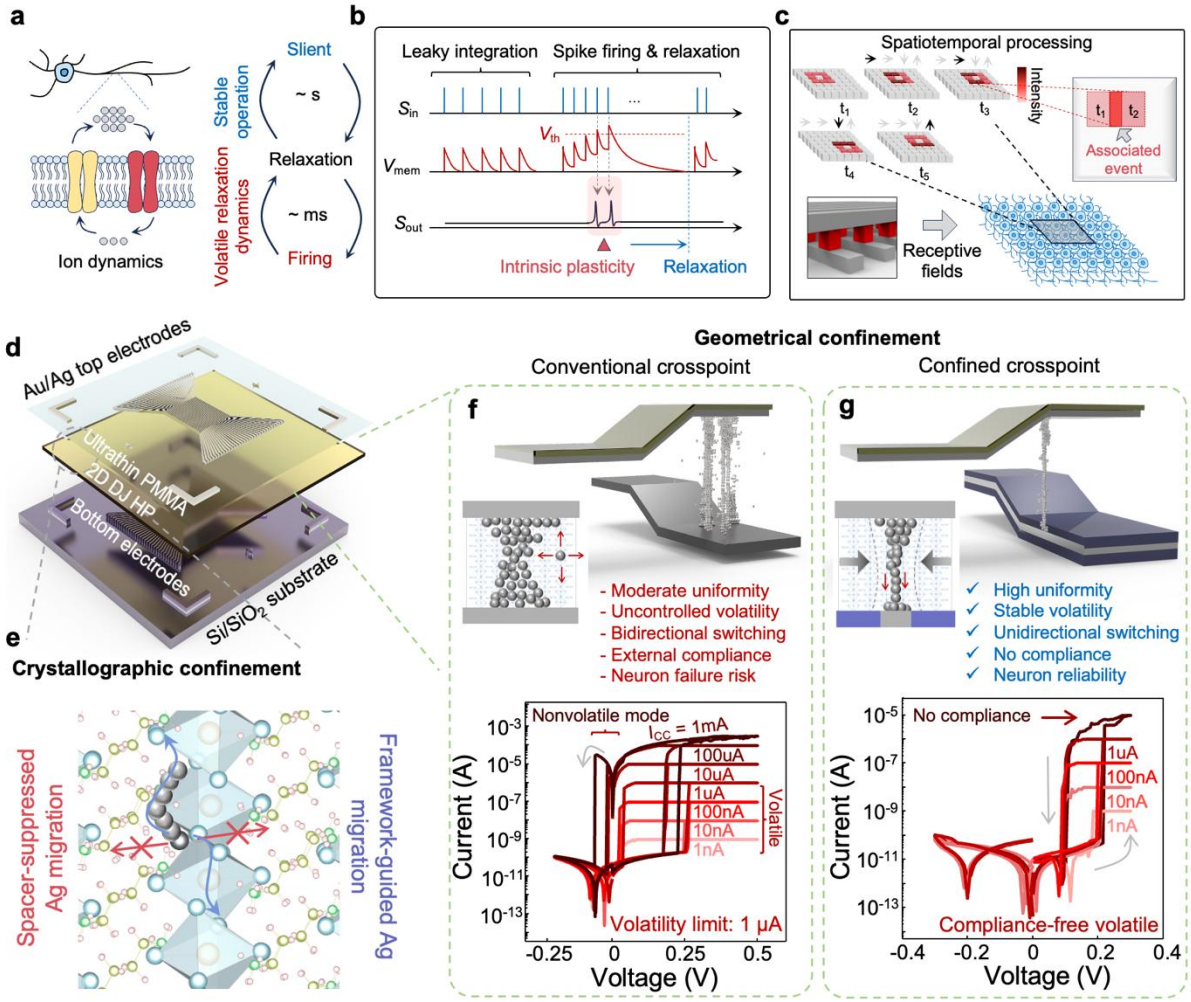


Figure 1. Three-dimensional junction engineering for reliable diffusive neuronal arrays. **a,** Schematic illustration of artificial neuronal operation based on dynamic ionic transport, in which electronic conduction and volatile ionic relaxation govern neuronal firing and recovery. **b,** Leaky integration, spike firing and subsequent relaxation under repeated temporal inputs, giving rise to intrinsic temporal plasticity. **c,** Schematic illustration of spatiotemporal signal processing in neuronal arrays through receptive-field activation and association of temporally correlated events. **d,** Crossbar-array (CBA) architecture based on two-dimensional (2D) Dion–Jacobson (DJ) halide perovskites with sidewall-defined switching regions. **e,** Anisotropic ion transport within the preferentially oriented DJ framework, in which organic spacer layers suppress ion migration across the layered framework while the inorganic slabs provide directional Ag-ion transport pathways toward the switching junction. **f,** Conventional crosspoint geometry showing spatially dispersed filament formation, poorly controlled volatility and compliance-dependent switching. **g,** Sidewall-defined junction geometry showing localized filament formation and self-limited, compliance-free volatile switching.

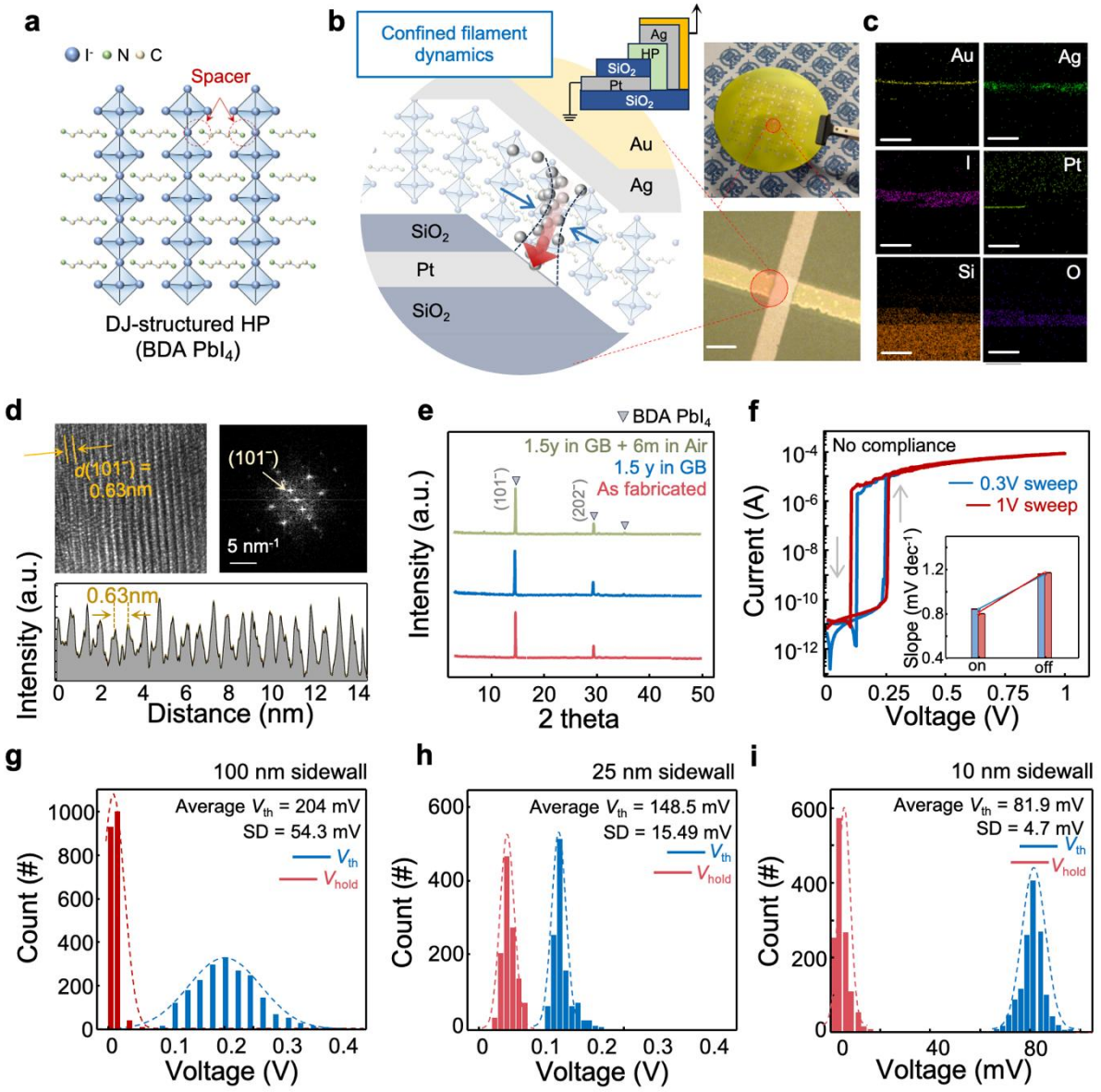


Figure 2. Three-dimensional junction engineering in halide perovskite diffusive neuronal devices. a, Crystal structure of the 2D DJ halide perovskite, illustrating anisotropic ion-migration pathways within the layered lattice. **b,** Schematic illustration of the diffusive neuronal device, in which junction engineering combines a sidewall-defined junction with the layered halide perovskite to establish a nanoscale switching volume for reliable volatile switching. A photograph demonstrating 4-inch wafer-scale fabrication, an enlarged optical micrograph of the device region and a cross-sectional device schematic are shown on the right. Scale bar, 100 μm. **c,** Cross-sectional EDS maps showing the spatial distributions of Au, Ag, I, Pt, Si and O. **d,** HRTEM image and corresponding FFT pattern of the 2D halide perovskite film. The measured lattice spacing of the (10−1) plane is 0.63 nm. The bottom panel shows the corresponding intensity line profile. **e,** XRD patterns of the 2D DJ halide perovskite measured immediately after fabrication, after 1.5 years of storage in a glovebox and after an additional 6 months of storage under ambient conditions, demonstrating crystallographic stability over 2 years. **f,** Current–voltage characteristics measured without external current compliance over different voltage sweep ranges. The inset shows the turn-on and turn-off switching slopes. **g–**

i, Distributions of threshold voltage (V_{th}) and hold voltage (V_{hold}) for devices with sidewall widths of 100 nm (**g**), 25 nm (**h**) and 10 nm (**i**). The mean V_{th} values are 204, 148.5 and 81.9 mV, with corresponding standard deviations (SD) of 54.3, 15.49 and 4.7 mV, respectively. Dashed curves show fits to the distributions.

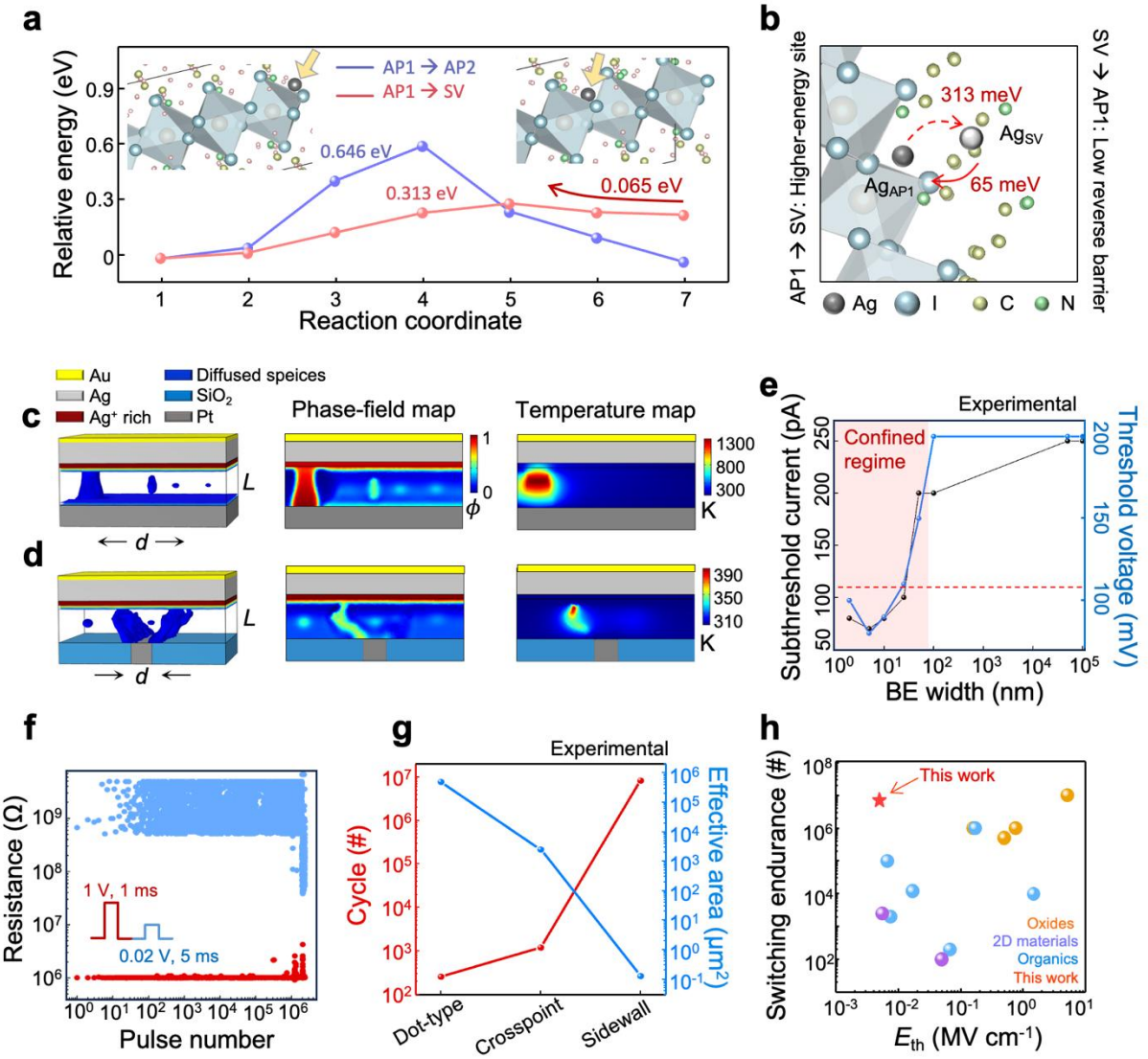


Figure 3. Ag-ion transport and geometrical confinement of conductive pathways in halide perovskite neurons. a, Nudged elastic band (NEB) calculations of Ag^+ migration-energy profiles along the AP1-to-AP2 and AP1-to-SV pathways in layered BDA–PbI_4, with energies referenced to AP1. The forward migration barriers are 0.646 and 0.313 eV, respectively. The SV-to-AP1 reverse barrier derived from the AP1-to-SV pathway is 0.065 eV. Insets show the corresponding atomic configurations. **b,** Schematic of Ag migration between the framework-associated apical iodide pocket AP1 and the higher-energy spacer-side site SV. The forward and reverse barriers are 313 and 65 meV, respectively. **c,** Multiphysics simulation of a wide-junction device, showing dispersed conductive pathways accompanied by extensive Joule heating. **d,** Corresponding simulation of a sidewall-defined device under otherwise identical conditions, showing localized conductive pathway and suppressed Joule heating for stable device operation. **e,** Dependence of subthreshold current and threshold voltage on BE width,

identifying the geometrically confined operating regime. **f,** Pulsed endurance characteristics of the sidewall-defined device. **g,** Comparison of switching endurance and effective device area among device architectures. **h,** Benchmarking of threshold electric field and switching endurance against representative threshold-switching devices.

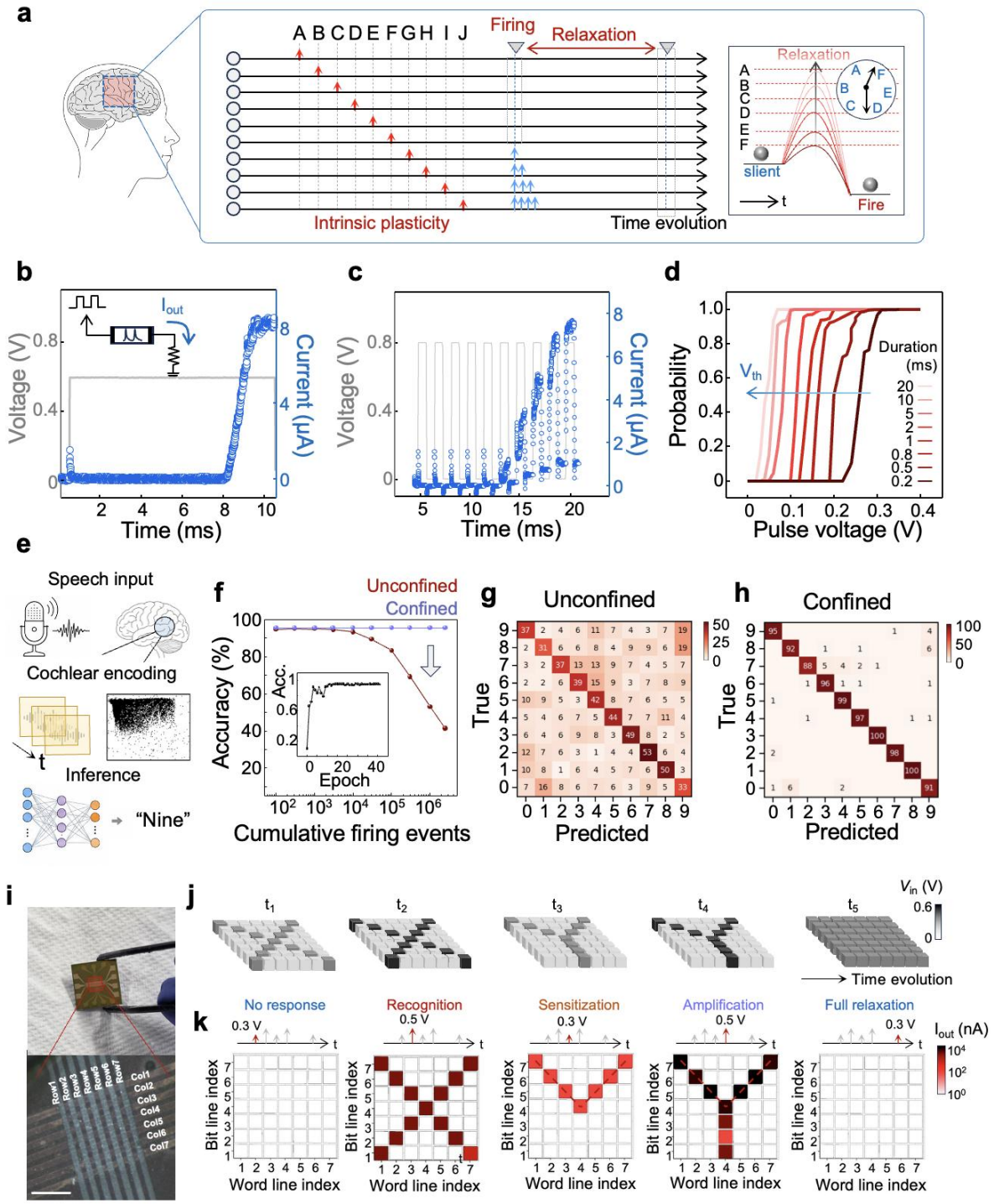


Figure 4. Temporal integration and context-dependent processing in halide perovskite neurons. a, Conceptual illustration of relaxation-mediated threshold modulation and intrinsic neuronal plasticity. Residual ionic configurations following stimulation transiently lower the

switching barrier for subsequent inputs before complete recovery. **b,** Delayed firing under a single prolonged voltage pulse. The output current initially remains low and then rises abruptly after a finite delay. The inset shows the measurement configuration for output-current readout. **c,** Integrate-and-fire operation under repeated voltage pulses of identical amplitude. Temporal integration produces firing after successive inputs. Grey traces in **b,c** indicate input-voltage pulses, and blue traces indicate output current. **d,** Firing probability as a function of pulse voltage for different pulse durations, showing a duration-dependent shift in the firing threshold. **e,** Schematic of the device-aware auditory classification benchmark using Spiking Heidelberg Digits (SHD) cochlear spike inputs. **f,** Simulated classification accuracy as a function of cumulative firing events after fixed readout training. The inset shows classification accuracy as a function of training epoch before device-aware inference. **g,h,** Confusion matrices after repeated event-driven operation for unconfined (**g**) and confined (**h**) volatile switching. **i,** Photograph of the fabricated neuronal array and enlarged optical micrograph of the crossbar region used for array-level characterization. Scale bar, 300 μm. **j,** Sequential input-voltage maps applied to the 7 × 7 crossbar array. Successive inputs from t_1 to t_4 were separated by 1 ms, and t_5 corresponds to complete relaxation after 50 ms. The colour scale indicates input voltage. **k,** Corresponding output-current maps showing no response under subthreshold stimulation, recognition of an X-shaped pattern, context-induced sensitization, suprathreshold amplification and recovery after complete relaxation. The colour scale indicates output current.

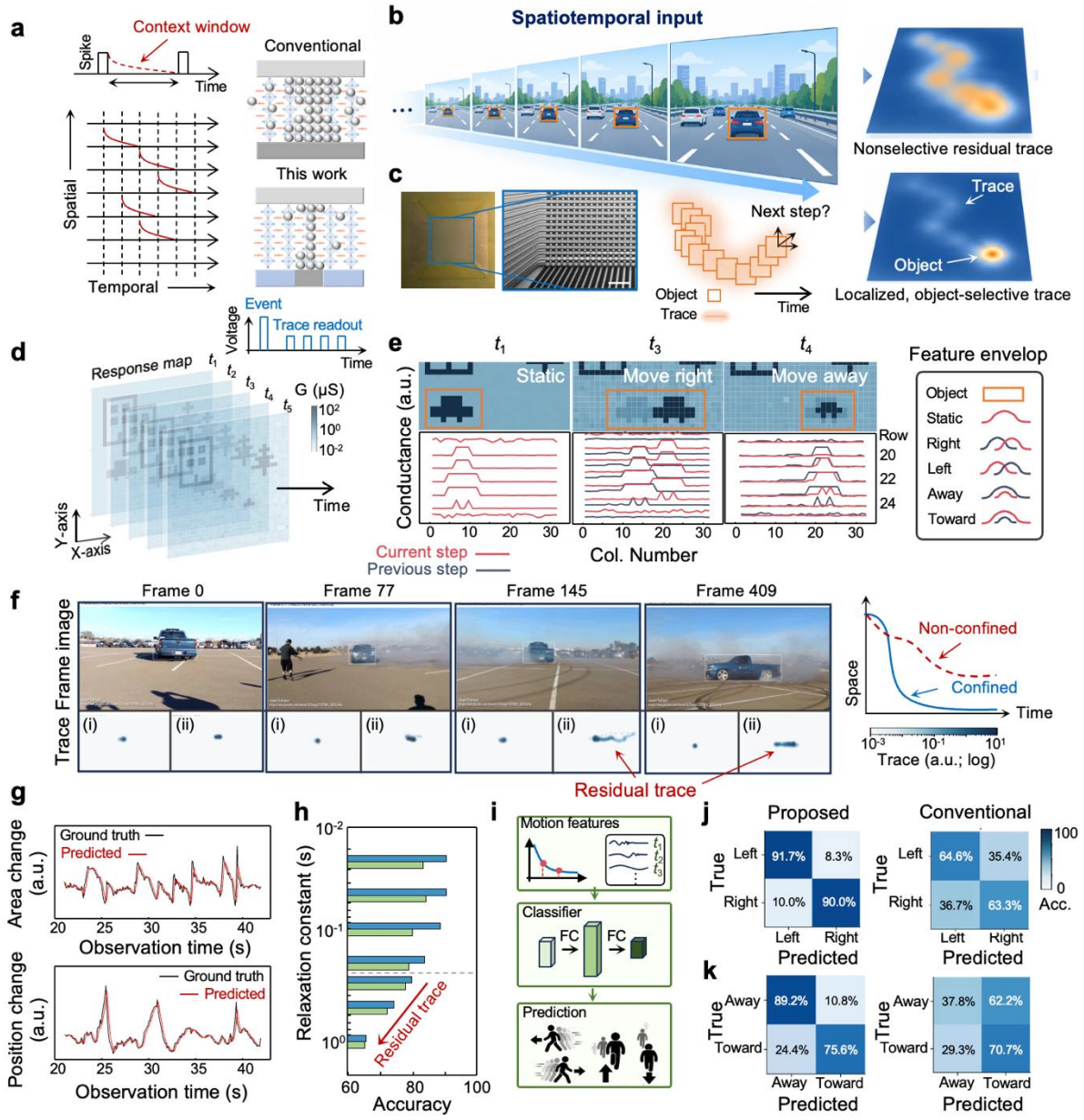


Figure 5. On-chip physical time surfaces for motion encoding and device-aware prediction. a, Conceptual illustration of transient context encoding through volatile relaxation, comparing spatially dispersed residual activity in conventional neurons with localized activity in the proposed neurons. **b**, Schematic of sequential visual inputs and the resulting temporal traces, illustrating nonselective residual accumulation and localized, object-selective encoding. **c**, Photograph of the fabricated 32 × 32 neuronal crossbar array (left) and scanning electron microscopy (SEM) image of the array region (right). **d**, Experimentally measured conductance maps demonstrating on-chip physical time surfaces that encode recent input history. The inset shows the measurement scheme using event pulses and trace-readout pulses. **e**, Measured spatial conductance profiles for a static object, rightward movement and movement away from the observer. Red and blue curves represent the current and preceding steps, respectively. The schematic on the right illustrates feature profiles associated with different motion states. **f**, Representative frames from the GOT-10k sequence and corresponding simulated temporal

maps for confined (i) and non-confined (ii) neuronal responses. The confined neuronal response preferentially retains recent object traces, whereas the non-confined response accumulates older traces that interfere with prediction of the immediate motion direction. The schematic on the right illustrates the corresponding spatial and temporal relaxation profiles. **g**, Reference and predicted changes in apparent object area and horizontal position during the GOT-10k sequence. **h**, Simulated motion-classification accuracy as a function of the neuronal relaxation time constant. The performance dependence on relaxation time reflects the balance between short-term motion memory and interference from persistent residual traces. **i**, Schematic of the motion-classification pipeline. Motion features extracted from the temporal response are converted into feature vectors and classified using a fully connected neural network into left, right, toward and away motion states. **j,k**, Confusion matrices comparing the proposed and conventional neuronal responses for left–right motion classification (**j**) and away–toward motion classification (**k**). Cell values indicate row-normalized classification percentages.

Supplementary Files

This is a list of supplementary files associated with this preprint. Click to download.

- Supplementaryinformation3Halidekimetal.docx